

The Multi-modality Cell Segmentation Challenge: Towards Universal Solutions

Jun Ma, Ronald Xie, Shamini Ayyadury*, Cheng Ge*, Anubha Gupta*, Ritu Gupta*, Song Gu*, Yao Zhang*, Gihun Lee, Joonkee Kim, Wei Lou, Haofeng Li, Eric Upschulte, Timo Dickscheid, José Guilherme de Almeida, Yixin Wang, Lin Han, Xin Yang, Marco Labagnara, Sahand Jamal Rahi, Carly Kempster, Alice Pollitt, Leon Espinosa, Tãm Mignot, Jan Moritz Middeke, Jan-Niklas Eckardt, Wangkai Li, Zhaoyang Li, Xiaochen Cai, Bizhe Bai, Noah F. Greenwald, David Van Valen, Erin Weisbart, Beth A. Cimini, Zhuoshi Li, Chao Zuo, Oscar Brück, Gary D. Bader, and Bo Wang

Abstract

Cell segmentation is a critical step for quantitative single-cell analysis in microscopy images. Existing cell segmentation methods are often tailored to specific modalities or require manual interventions to specify hyperparameters in different experimental settings. Here, we present a multi-modality cell segmentation benchmark, comprising over 1500 labeled images derived from more than 50 diverse biological experiments. The top participants developed a Transformer-based deep-learning algorithm that not only exceeds existing methods, but can also be applied to diverse microscopy images across imaging platforms and tissue types without manual parameter adjustments. This benchmark and the improved algorithm offer promising avenues for more accurate and versatile cell analysis in microscopy imaging.



INTRODUCTION

Cell segmentation is a fundamental task that is universally required for biological image analysis across a large number of different experimental settings and imaging modalities. For example, in multiplexed fluorescence image-based cancer microenvironment analysis, cell segmentation is the prerequisite for the identification of tumor sub-types, composition, and organization, which can lead to important biological insights [1]–[3]. However, the development of a universal and automatic cell segmentation technique continues to pose significant challenges due to the extensive diversity observed in microscopy images. This diversity arises from variations in cell origins, microscopy types, staining techniques, and cell morphologies. Recent advances [4], [5] have successfully demonstrated the feasibility of automatic and precise cellular segmentation for specific microscopy image types and cell types, such as fluorescence and mass spectrometry images [6], [7], differential interference contrast images of platelets [8], bacteria images [9] and yeast images [10], [11], but the selection of appropriate segmentation models remains a non-trivial task for non-expert users in conventional biology laboratories.

Efforts have been made towards the development of generalized cell segmentation algorithms [9], [12], [13]. However, these algorithms were primarily trained using datasets consisting of gray-scale images and two-channel fluorescent images, lacking the necessary diversity to ensure robust generalization across a wide range of imaging modalities. For example, the segmentation models have struggled to perform effectively on RGB images, such as bone marrow aspirate slides stained with Jenner-Giemsa. Furthermore, these models often require manual selection of both the model type and the specific image channel to be segmented, posing challenges for biologists with limited computational expertise.

Biomedical image data science competitions have emerged as an effective way to accelerate the development of cutting-edge algorithms [14], [15]. Several successful competitions have been specifically organized for microscopy image analysis, such as the cell tracking challenge (CTC) [16], [17] and the Data Science Bowl (DSB) challenge [18]. These competitions have played a crucial role in expediting the adoption of modern machine learning and deep learning algorithms in biomedical image analysis. However, it is worth noting that these challenges have primarily focused on a limited subset of microscopy image types. For example, the CTC primarily concentrated on label-free images, thereby excluding stained images such as multiplexed immunofluorescent images. Similarly, the DSB challenge emphasized nucleus segmentation in fluorescent and histology images while disregarding phase-contrast and differential interference contrast images. Consequently, the algorithms developed through these competitions are often tailored to handle only specific types of microscopy images, limiting their generalizability. Moreover, the evaluation metrics used in these challenges predominantly prioritize segmentation accuracy, while neglecting algorithm efficiency. As a result, the pursuit of higher accuracy scores often leads to the adoption of computationally demanding approaches. For instance, the CTC top-performing algorithms employed customized models for each dataset in the cell segmentation task, while the DSB

A full list of affiliations appears at the end of the paper. * denotes equal contribution (ranked based on the last name). Corresponding Author: Bo Wang. E-mail: bowang@vectorinstitute.ai.

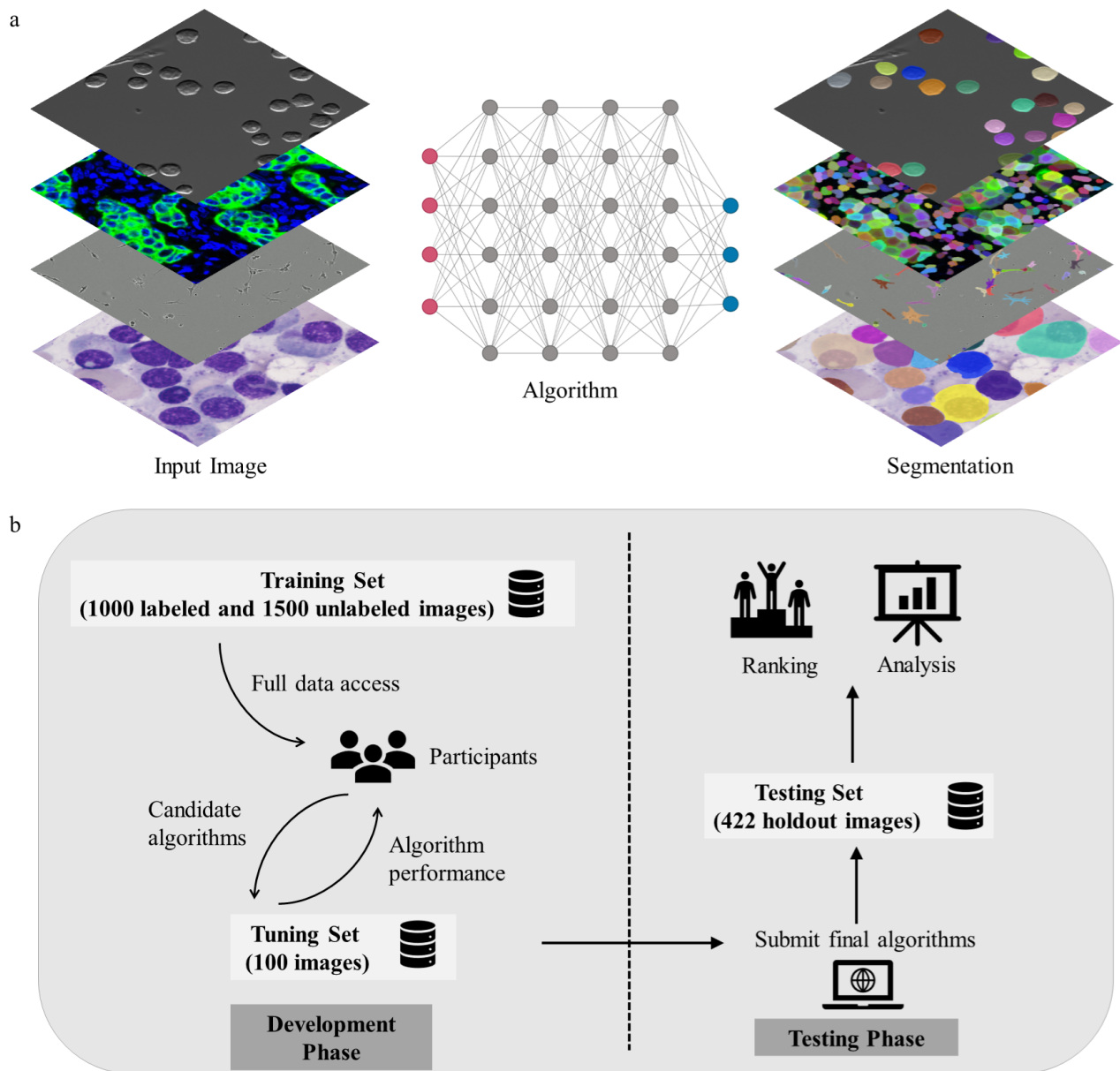


Fig. 1. Overview of the challenge task and pipeline. **a**, The challenge aims to facilitate the development of universal cell segmentation algorithms that can segment a wide range of microscopy images without manual intervention. **b**, The challenge contains two phases. During the development phase, participants develop automatic segmentation algorithms based on 1000 labeled images and 1500 unlabeled images. The algorithms can be evaluated on a tuning set with 100 images and the online evaluation platform will automatically return back the quantitative performance. During the testing phase, each team can submit one algorithm via the Docker container as the final solution, which is independently evaluated on the holdout testing set with 422 images to obtain ranking results.

winning algorithm used an ensemble of 32 models. Such resource-intensive strategies hinder the wide deployment of these algorithms in biology practice.

To overcome the aforementioned limitations and foster the development of universal and efficient cell segmentation methods for microscopy images, we took the initiative to organize a global challenge at the Conference on Neural Information Processing Systems (NeurIPS). As one of the largest international conferences in the field of artificial intelligence (AI), NeurIPS provided an ideal platform for this endeavor. Participants in the challenge were provided with a diverse training set and a separate tuning set to develop and refine their cell segmentation algorithms. During the testing phase, participants were required to package their algorithms as Docker containers, enabling the challenge organizers to evaluate them on a carefully curated holdout testing set on the same computing platform. Importantly, the holdout testing set incorporated images from new biological experiments, aiming to assess the algorithms' ability to generalize effectively to previously unseen data. Additionally, the testing set included two whole-slide images, serving as a means to evaluate the algorithms' suitability for handling large-scale images. Different from existing challenges that focused on specific microscopy image types, this initiative represents the first instance where cell segmentation algorithms were challenged to efficiently handle a

broad spectrum of microscopy images with one single model and generalize to new images without manual intervention.

RESULTS

Challenge design: towards universal and efficient cell segmentation algorithms

The primary objective of this challenge was to benchmark universal algorithms capable of accurately segmenting cells from a wide range of microscopy images obtained from various imaging platforms and tissue types, without requiring additional parameter tuning (Fig. 1a). The algorithms were expected to operate in a fully automatic manner, generating cell instance masks where each cell is assigned a unique label. The challenge comprised two phases (Fig. 1b). In the development phase, participants were provided with a dataset consisting of 1000 microscopy images, each accompanied by annotated cell masks. Recognizing the potential benefits of leveraging unlabeled data to enhance model performance [19], we also made an additional set of 1500 unlabeled images available for participants to utilize. Participants were given the flexibility to decide whether to incorporate this unlabeled dataset into their algorithms. This setup aligns with real-world scenarios encountered in biological research, where only a limited number of labeled images are typically available alongside a wealth of unlabeled images.

To facilitate timely model validation, a separate tuning set containing 100 images was provided to participants, but the corresponding annotations were not disclosed. Instead, we established an online evaluation platform, enabling participants to upload their segmentation results and receive evaluation scores. These scores were made publicly available on a leaderboard, enabling direct comparisons among participants and their algorithms throughout the development phase.

In the subsequent testing phase, the top 30 teams, as ranked on the public tuning set leaderboard, were invited to make the testing submission. The testing set remained hidden from participants, aiming to avoid potential label leaking and cheating. To ensure standardized evaluation, participants were required to package and submit their algorithms as Docker containers. Challenge organizers run the submitted Docker containers on the holdout testing set comprising 422 microscopy images. Out of the 30 invited top teams, 28 teams made successful submissions, while one team did not submit and another team submitted after the deadline, making their submission ineligible for final ranking. To ensure a fair comparison, we executed the Docker containers sequentially on the same workstation. The running time for each image was recorded, alongside the corresponding segmentation accuracy score. Both of them were used for the final ranking and subsequent analysis of the algorithms (Methods).

Challenge data: a large and diverse multi-modality microscopy image dataset

Data diversity plays a pivotal role in constructing generalist microscopy image segmentation models [20]. In this challenge, we incorporated the diversity of microscopy images from four dimensions: cell origins, staining methods, microscope types, and cell morphologies (Fig. 2a). First, the origin of cells in microscopy images varies significantly, as they can derive from diverse tissues or exist within cell cultures under various conditions. This introduces considerable variability, as cells within tissues tend to be densely packed and spatially organized, whereas cells in culture are often sparsely distributed and randomly positioned. Second, the choice of staining methods, such as Jenner-Giemsa in brightfield microscopy or the utilization of specific antibodies in fluorescent microscopy, further contributes to the diversity by highlighting different cellular structures or proteins. Third, the use of different microscope types, such as brightfield, fluorescent, phase-contrast (PC), and differential interference contrast (DIC), introduces substantial differences in image characteristics, textures, and associated artifacts. Fourth, cell morphologies exhibit substantial variations across different cell types. While most cells tend to have a round shape, certain cells may display elongated or irregular shapes.

We curated a diverse microscopy image dataset by collecting images (and annotation if available) from over 20 biology laboratories, including more than 50 different biological experiments (Supplementary Table 1-3). This comprehensive dataset encompassed four common microscopy image modalities: brightfield, fluorescent, phase-contrast (PC), and differential interference contrast (DIC). The challenge garnered significant interest and participation, attracting over 400 participants from 37 different countries, reflecting the global reach and impact of the challenge (Fig. 2b). The training set contained a total of 1000 images, with 300 images each in the brightfield and fluorescent categories, and 200 images each in the PC and DIC categories (Fig. 2c). The annotated dataset contained 12,702 cells in brightfield images, 130,194 cells in fluorescent images, 9,504 cells in PC images, and 16,091 cells in DIC images (Fig. 2d). Notably, the higher cell count in fluorescent images compared to other modalities can be attributed to the denser distribution of cells observed in the collected fluorescent images.

Fig. 2e shows four microscopy images randomly selected from each modality in the training set and testing set. In order to assess the algorithm's generalization capabilities, all testing images were sourced from new biological experiments, including some that featured previously unseen tissues or cell types not present in the training set. The testing set consisted of 120 brightfield images, 122 fluorescent images, 120 phase-contrast (PC) images, and 60 differential interference contrast (DIC) images (Fig. 2f). These quantities were determined based on the available images collected for the challenge. The number of cells in the testing set was comparable to or greater than that of the training set (Fig. 2g). Additionally, the fluorescent image subset of the testing set included two whole-slide images (WSIs), which served the purpose of evaluating the algorithms' ability in handling large-scale imaging datasets.

In comparison to previous datasets utilized in cell segmentation challenges [17], [21] and nucleus segmentation challenges [18], our dataset exhibits significantly enhanced diversity and encompasses a larger number of labeled cells. This

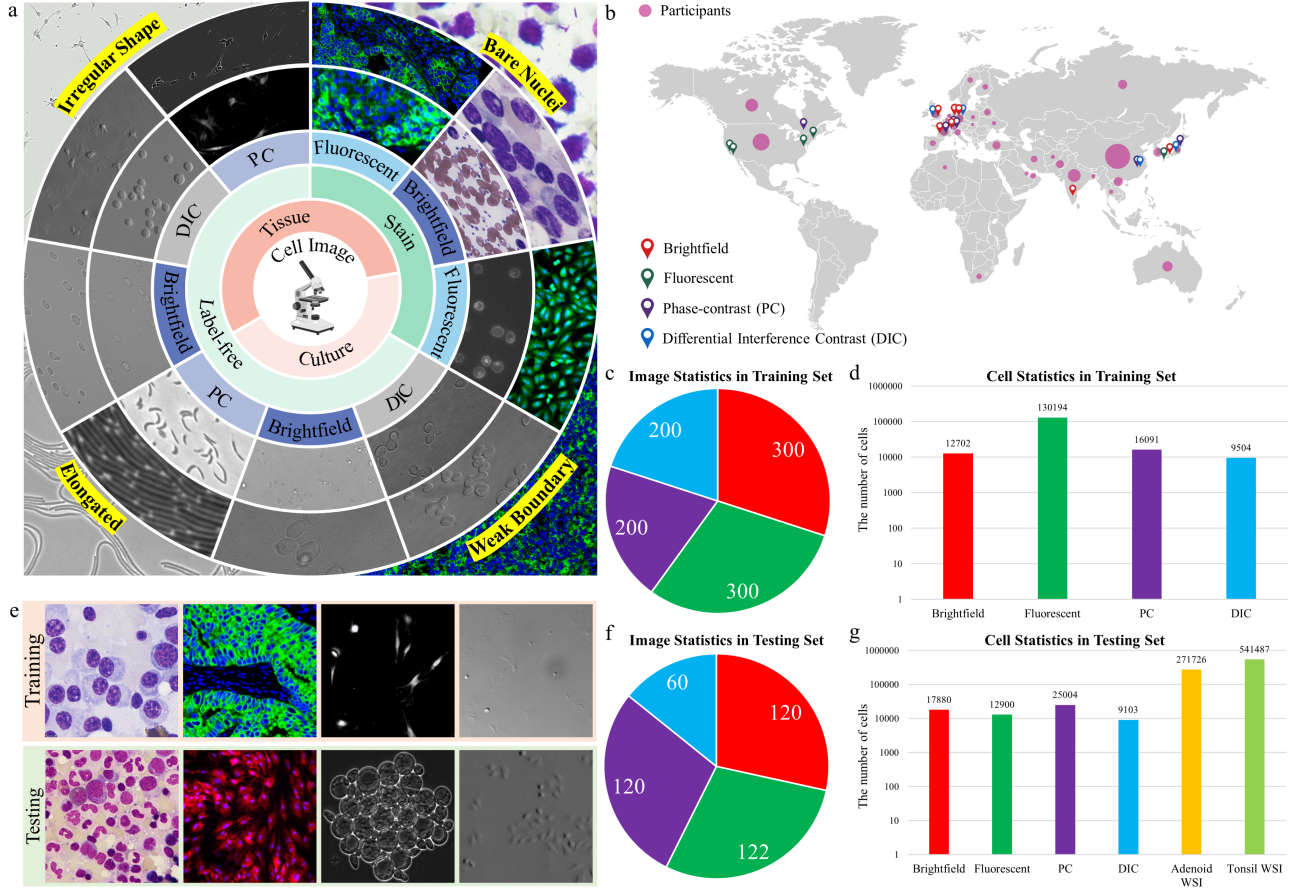


Fig. 2. **Dataset overview.** **a**, The challenge provides a diverse microscopy image dataset that includes tissue cells, cultured cells, label-free cells, stained cells, and different microscopes (i.e., brightfield, fluorescent, phase-contrast (PC), and (Differential Interference Contrast) DIC). **b**, The dataset source and the challenge participant distribution. In each country, the circle size is proportional to the number of participants. **c**, The number of images in the training set. **d**, The number of labeled cells in the training set. **e**, Randomly selected examples (from left to right: brightfield, fluorescent, PC, and DIC images) from the training set (the 1st row) and testing set (the 2nd row). **f**, The number of images in the testing set. **g**, The number of cells in the testing set. There are two fluorescent whole-slide images (WSI) in the testing set.

extensive dataset serves as a fertile ground for fostering the development of advanced cell segmentation algorithms, enabling researchers to explore and innovate in the field.

Algorithm overview: the Transformer-based algorithm achieved superior performance

All algorithms in this challenge employed deep learning-based approaches, a prevailing trend considering the remarkable performance achieved in various specific cell segmentation tasks [6], [11], [17], as well as in recent generalist cell segmentation algorithms [9], [13]. Existing algorithms predominantly relied on Convolutional Neural Networks (CNNs) such as U-Net [22], [23] and DeepLab [24]. However, it is worth noting that these CNN-based cell segmentation models exhibited limited generalization capability when confronted with the task of segmenting diverse images without additional human intervention, such as manual selection of channels or model fine-tuning, as demonstrated in the following sections.

In contrast, Transformers [25], a new type of deep learning network integrating attention mechanisms for feature extraction, have exhibited robust performance and generalization capabilities across various computer vision tasks [26], [27]. However, the potential of Transformers in biological image analysis remains relatively unexplored [20], [28]. Distinguished from existing benchmarks [17], [18], our challenge provided a significantly larger and more diverse microscopy image dataset. Leveraging this unprecedented dataset and a meticulously designed benchmark, Transformer-based deep learning models emerged as exceptional algorithms and achieved notably superior performance.

Best-performing algorithm. Lee et al. [29] (T1-osilab) proposed a Transformer-based framework to harmonize model-centric and data-centric approaches. The model architecture used SegFormer [30] and multiscale attention network [31] as the encoder and decoder. The SegFormer encoder was a hierarchical Transformer, enabling the extraction of both coarse and fine-grained features. The decoder contained position-wise attention blocks and multiscale fusion attention blocks for feature map fusion. The model output comprised two separate heads for cell recognition and distinction. The model underwent a two-step training process. It was first pre-trained on public microscopy images and then fine-tuned on the challenge dataset with cell-aware data augmentation. Additionally, cell memory reply [32], concatenating the images from

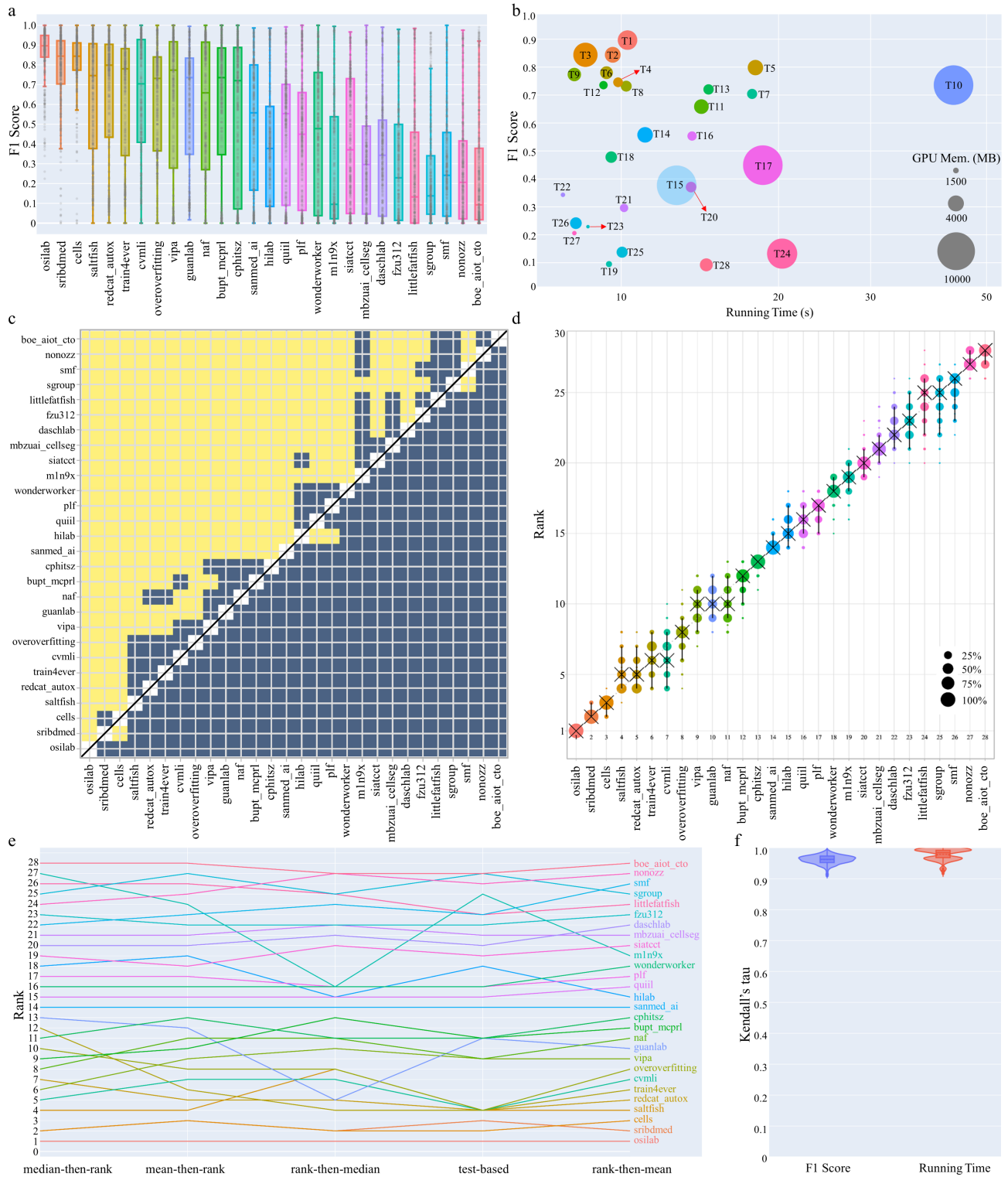


Fig. 3. Evaluation results of 28 algorithms on the holdout testing set. **a**, Dot and box plot of the F1 scores on the testing set. The box plots display descriptive statistics across all testing cases, with the median value represented by the horizontal line within the box, the lower and upper quartiles delineating the borders of the box, and the vertical black lines indicating the 1.5 interquartile range. **b**, The top algorithms achieve a good trade-off between segmentation accuracy (y-axis) and efficiency (x-axis). The circle size is proportional to GPU memory consumption. **c**, Pairwise significant test results (one-sided Wilcoxon signed rank test) show that the winning algorithm is significantly better than the other algorithms. **d**, Blob plot for visualizing ranking stability based on bootstrap sampling. The median area of each blob is proportional to the relative frequency of achieved ranks across 1000 bootstrap samples. The median rank for each algorithm is indicated by a black cross. 95% bootstrap intervals across bootstrap samples are indicated by black lines. **e**, The winning algorithm holds the first place across five different ranking schemes. **f**, The high Kendall's tau scores indicate that the ranking results are stable.

TABLE 1

Characteristics of top three best-performing algorithms in pre-processing, data augmentation, network architecture, and post-processing. Abbreviation: Intensity Normalization (IN), Patch Sampling (PS), Intensity and Spatial data augmentation (IS), External Datasets (ED), Unlabeled Data (UD), Non-Maximum Suppression (NMS), Test-time Augmentation (TTA). ‘-’ denotes it is not used.

Team	Pre-processing		Data Augmentation				Network Architecture		Post-processing
	IN	PS	IS	ED	UD	Others	Encoder Backbone	Decoder Heads	
T1 osilab [29]	✓	✓	✓	✓	-	Cell-wise intensity perturbation; Boundary exclusion; Oversample minor modality;	SegFormer	Cell probability head; Gradient fields regression head;	Gradient tracking; Exclud small cells; Fill holes; TTA;
T2 sribdmed [33]	✓	✓	✓	✓	✓	-	ConvNeXt	Cell probability head; Radial distance head; Gradient fields regression head;	NMS; Watershed;
T3 cells [35]	✓	✓	✓	✓	✓	Cell-wise rescaling;	ResNeXt-101	Classification head; Contour regression head; Local refinement regression head; Boundary uncertainty estimation head;	Convert contours to masks; Region growing;

the pre-training and fine-tuning datasets in each mini-batch, was used to avoid catastrophic forgetting during fine-tuning (Methods).

Second-best-performing algorithm. Lou et al. [33] (T2-sribdmed) first divided the images into four distinct categories based on low-level image features (e.g., intensities) in an unsupervised way. Then, class-wise cell segmentation models were trained for each category. The model employed U-Net-like architecture where ConvNeXT [34] was used as the building blocks. To address the diverse cell morphologies, two distinct decoder heads were employed. One decoder predicted the cell distance map and semantic map, effectively segmenting round-shaped cells, while the other decoder predicted the cell gradient map to handle cells with irregular shapes. The training process involved pre-training the model on the entire dataset, followed by fine-tuning on each of the four categories, resulting in the creation of four models. During inference, the image was initially classified into one of the four categories, and subsequently, the corresponding model was used to perform the segmentation process (Methods).

Third-best-performing algorithm. Upschulte et al. [35] (T3-cells) designed an uncertainty-aware contour proposal network, employing ResNeXt-101 [36] to extract multiscale features from images, which were then processed through four decoder heads. A classification head identified potential cell locations, while a contour regression head predicted sparse cell contours. To further improve accuracy, a refinement regression head was employed to revise the pixels within the cell contour. In addition, they incorporated an uncertainty head to estimate prediction confidence, which played a crucial role in the non-maximum suppression post-processing. This incorporation of uncertainty information effectively facilitated the removal of redundant contour proposals and enhanced segmentation accuracy (Methods).

Other strategies. Table 1 summarizes the strategies employed by the top three teams. Given the considerable variation in image intensity and size across different modalities, all these teams adopted intensity normalization techniques (e.g., scaling the intensity to [0, 255]) during pre-processing and opted for patch-based sampling for model training. To enhance the model generalization ability and mitigate the risk of overfitting, diverse data augmentation methods were utilized. In addition to using external datasets, teams T2 and T3 leveraged the unlabeled data for model pre-training. Despite the common adoption of an encoder-decoder framework to construct networks, the top teams showcased variations in their choice of backbone networks and decoder heads. Consequently, the corresponding post-processing methods exhibited diversity.

Next, we present the quantitative results of the 28 algorithms on the holdout testing set. Fig. 3a (Supplementary Table 4) shows a comparative view of F1 scores across 28 algorithms on the testing set. The scores are presented in the form of a dot and box plot, offering insights into both their central tendency and dispersion of the scores. The top three algorithms surpass other algorithms by a clear margin, resulting in median F1 scores of 89.7% (interquartile range (IQR): 84.0-94.9%), 84.4% (IQR: 70.4-92.2%), and 84.4% (IQR: 77.3-91.1%), respectively. Of particular note is the performance of the winning algorithm (T1-osilab). It stands apart not merely for its superior median F1 score, but also for the reduced number of outliers in its score distribution, suggesting a heightened level of robustness in its performance.

The bubble plot (Fig. 3b) presents the median F1 score, running time, and the maximum GPU memory consumption of 28 algorithms, which can provide insights into the trade-off between algorithm accuracy and efficiency. Most algorithms optimized the efficiency, enabling them to finish the inference within 13s. It is essential to mention that this time metric also included the Docker starting time, hence the actual inference time is considerably shorter. For instance, the best-performing algorithm (T1-osilab) achieved an inference time of approximately 2 seconds for an image size of 1000 × 1000. Additionally, the median maximum GPU memory consumption was 3099MB (approximately \$500), suggesting that these algorithms are affordable for practical deployment. This favorable combination of accuracy and efficiency makes them well-suited for

real-world applications in biological image analysis.

We also performed a statistical significance analysis for the 28 algorithms (Fig. 3c). Each team was compared with the other teams based on the one-sided Wilcoxon signed rank test. Yellow shading indicates that the F1 scores of the algorithm on the x-axis are significantly superior ($p < 0.05$) to those from the algorithm on the y-axis, while blue shading indicates no significant difference between the two algorithms. The winning algorithm is significantly better than all the others. The 2nd algorithm and the 3rd algorithm obtain comparable performances with no significant differences, but they are significantly superior to other teams.

Furthermore, we analyzed the ranking stability based on bootstrap sampling (1000 times). The results are visualized by blob plot (Fig. 3d). The blob area is proportional to the relative frequency of achieved ranks across the bootstrap samples and the median rank for each algorithm is indicated by a black cross. The winning algorithm has a blob area of 100%, indicating that it outperforms other algorithms in all the bootstrap samples. The 2nd and 3rd best-performing algorithms still obtain better rank than other algorithms with a clear gap while the 2nd best-performing algorithm has a lower median rank than the 3rd best-performing algorithm. Moreover, we compared the ranks of the 28 algorithms based on different ranking schemes (Fig. 3e): median-then-rank, mean-then-rank, rank-then-median, statistical significance test-based ranking, and rank-then-mean (Methods). The winning algorithm consistently ranks first place across all the ranking schemes, while most other teams have fluctuations in terms of the rank.

Finally, we analyzed the ranking stability of the employed metrics. The ranking list based on the full testing set is pairwise compared with the ranking lists based on the individual sample in the 1000 bootstrap samples. Kendall's tau correlation is computed as a quantitative metric (Fig. 3f). It can be found that Kendall's τ scores are very close to 1 for both F1 scores and running time, indicating a high degree of ranking agreement. Additionally, the compact distributions of these scores further confirm the stability of the ranking results with respect to sampling variability. These findings provide robust evidence that the obtained rankings are highly consistent and reliable across different samples.

The best-performing algorithms outperform state-of-the-art cell segmentation algorithms

In order to demonstrate the advancement of the winning algorithm beyond the state-of-the-art (SOTA) in cell segmentation, we compared the top three best-performing algorithms to three existing generalist algorithms: Cellpose [12], Omnipose [9], and Cellpose 2.0 [13], as well as the top-performing algorithm KIT-GE [37] from the CTC cell segmentation task [17]. We trained KIT-GE and Cellpose 2.0 on the challenge training set and then predicted the testing images. The Cellpose 2.0 model was initialized with the default pre-trained Cellpose model. The pre-trained generalist models in Cellpose and Omnipose were directly employed to segment the testing images (Methods). Notably, these algorithms share the commonality of being constructed on CNN architectures, such as U-Net [22].

Fig. 4a (Supplementary Table 5) illustrates the F1 scores of these seven methods on the testing set, revealing that the top three best-performing algorithms achieved significantly higher accuracy compared to the existing SOTA algorithms. Among the four SOTA algorithms, the pre-trained Cellpose model emerged as the top performer with a median F1 score of 65.3% (IQR: 36.7-82.4%). Surprisingly, the Cellpose 2.0 model, trained on the challenge dataset, exhibited a lower performance (60.2% (IQR: 17.4-87.6%)) compared to the pre-trained Cellpose model, contrary to initial expectations. To investigate the potential reason for this unexpected performance decrease during fine-tuning, we conducted further analysis, particularly focusing on the segmentation performance across different modalities.

Fig. 4b presents the results on the brightfield images, where the top two best-performing algorithms remained at the forefront, achieving median F1 scores of 91.4% (IQR: 88.0-94.9%) and 91.0% (IQR: 86.1-93.8%), respectively. The Cellpose 2.0 model exhibited comparable performance to the third-best-performing algorithm, achieving a significant improvement of 22% in median F1 score over the pre-trained Cellpose model, as anticipated due to its training on the challenge dataset. Fig. 4c shows the results on the fluorescent images, where the third best-performing algorithm outperformed others with a median F1 score of 80.8% (IQR: 71.6-91.5%), followed by the best-performing algorithm and the pre-trained Cellpose model. However, the F1 score of Cellpose 2.0 declined substantially by 24%. This decrease can be attributed to the testing images being from new cell types not present in the training set, signifying a case of catastrophic forgetting during the fine-tuning of Cellpose, a common occurrence in transfer learning [38].

In Fig. 4d, the results for PC images demonstrated that the top three best-performing algorithms maintained their superiority in this category, achieving median F1 scores of 93.6% (IQR: 87.9-96.4%), 88.8% (77.7-96.4%), and 90.3% (84.3-95.0%), respectively. The CTC challenge's top-performing segmentation algorithm, KIT-GE, excelled in PC images due to its design for label-free images and the relatively simple segmentation of round-shaped cells. However, Cellpose 2.0 showed decreased performance compared to the pre-trained Cellpose model due to catastrophic forgetting, as the testing set included unseen images. Fig. 4e shows the results on DIC images with the top three best-performing algorithms once again achieving the highest performance, achieving median F1 scores of 86.8% (IQR: 83.5-88.0%), 75.0% (IQR: 68.9-78.1%), and 80.3% (77.2-85.1%), respectively. While Omnipose yielded the best performance among the SOTA methods with a median F1 score of 43.4% (IQR: 33.1-60.9), it still fell significantly behind the top three best-performing methods. Conversely, KIT-GE and Cellpose 2.0 struggled in this category, facing challenges due to the DIC testing images originating from entirely new biological experiments.

We further visualized segmentation examples of the seven algorithms to gain insights into their characteristics (Fig 4f, Supplementary Fig. 1). The top three best-performing algorithms demonstrated relatively robust results, with the best-performing algorithm (T1-osilab) displaying exceptional accuracy across diverse microscope types, cell types, and image

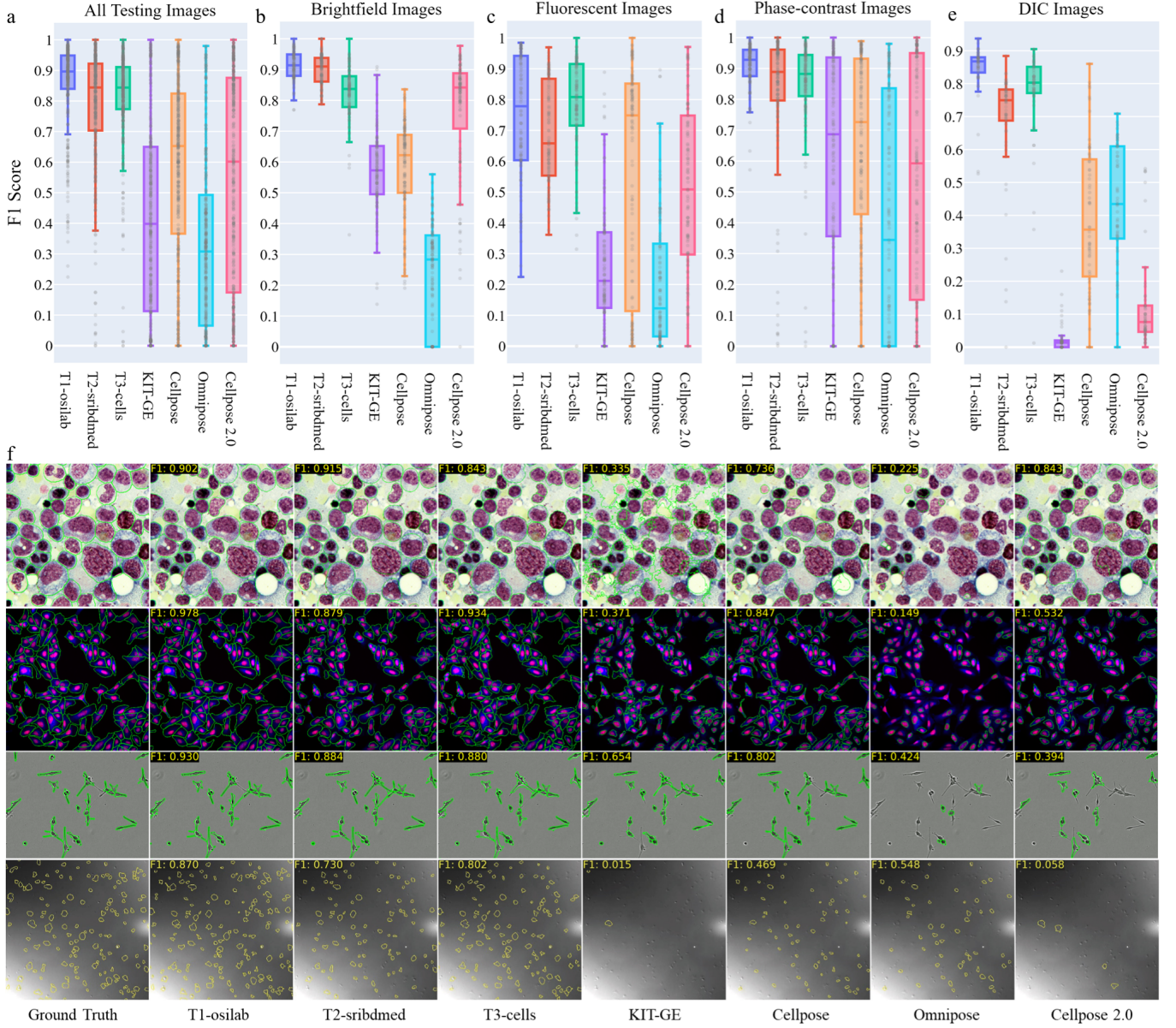


Fig. 4. Quantitative and qualitative comparison between the top three algorithms and state-of-the-art generalist cell segmentation algorithms: KIT-GE (top solution in the segmentation benchmark of the cell tracking challenge), Cellpose, Omnipose, and Cellpose 2.0. Dot and box plot of the F1 scores on the **a**, whole testing test; **b**, brightfield images; **c**, fluorescent images; **d**, phase-contrast images; **e**, DIC images. **f**, Example segmentation results of the four microscopy image modalities: brightfield, fluorescent, phase-contrast, and DIC images (from top to bottom).

contrasts. Notably, KIT-GE exhibited better performance on phase-contrast images than stained images, as it was designed based on a label-free challenge dataset. Nevertheless, KIT-GE struggled to segment DIC images from new biological experiments, indicating limited generalization ability in this context. The pre-trained Cellpose model outperformed Omnipose on most images, except for DIC images featuring numerous small objects with low contrasts. Additionally, Cellpose 2.0 surpassed the original Cellpose on brightfield images, exhibiting fewer segmentation errors. However, its performance suffered on other modalities that contained previously unseen images, leading to an increased number of missed cells and highlighting the issue of catastrophic forgetting.

DISCUSSION

The primary and arguably most significant observation in this challenge is the unequivocal superiority of the Transformer-based algorithm, which exhibited significantly enhanced performance compared to existing SOTA cell segmentation algorithms. Transformers offer several unique advantages compared to CNNs. First, Transformers [25] use self-attention mechanisms that can capture global context and long-range dependencies in images, while CNNs usually process local image patches. Second, Transformers have a larger model capacity than CNNs [26], enabling them to learn intricate patterns

and model nuanced relationships in images, which are essential for accurate cell segmentation. Third, Transformers excel in transfer learning settings, allowing the model to pre-train on large datasets and subsequently fine-tuned on specific downstream tasks or new datasets with limited annotations. Notably, this effective strategy was also successfully adopted by the winning algorithm.

The winning algorithm demonstrated a remarkable level of superiority compared to the leading algorithm from the CTC challenge, even after the latter was retrained on our dataset. This notable improvement can be attributed to the unparalleled diversity of the dataset. Unlike the CTC challenge dataset, which only comprised label-free images, our challenge dataset encompassed both labeled and label-free images. Furthermore, our challenge focused on universal segmentation algorithms, while the top-performing teams of the CTC challenge developed tailored models for each dataset [39], [40]. This fundamental difference in strategy likely contributed to the substantial performance gap.

In addition to the Transformer-based architecture, we also identified several useful strategies for achieving top performance. First, different from the typical detection-then-segmentation paradigm [41], multi-head outputs were employed by most of the top algorithms [29], [33], [35], which converted the instance segmentation task into distance map regression tasks and a cell foreground semantic segmentation task, followed by post-processing to merge the output as instance labels. This approach was conclusively demonstrated to be superior to the conventional detection-then-segmentation paradigm in this challenge. Another crucial aspect was the adoption of diverse and robust data augmentation techniques, which is important to improve the model generalization ability and reduce overfitting. In addition to commonly used global intensity augmentations (e.g., scaling, noise addition, and blurring) and spatial augmentations (e.g., rotation, zooming, flipping), participants introduced innovative augmentation methods. For example, Lee et al. [29] employed cell-wise random perturbations in image intensity, while Li et al. [42] used Mosaic data augmentation [43], enabling the model to learn object identification at varying scales. Moreover, employing efficient backbone networks, such as SegFormer [30] and ConvNext [34], offered a favorable accuracy-efficiency trade-off. The winning algorithm also demonstrated that the slide-window-based method was an efficient strategy for scalable inference (Supplementary Table 6). Specifically, the input image was partitioned into multiple smaller patches, and their predictions were subsequently stitched together to form the final label map. This method proved particularly crucial for whole-slide image segmentation, considering the inherent limitations of RAM and GPU memory in real practice.

Furthermore, we made a noteworthy observation concerning the commonly employed transfer learning algorithm, e.g., Cellpose 2.0 [13], which exhibited a phenomenon known as catastrophic forgetting. The original Cellpose model, pre-trained on a diverse array of microscopy images, demonstrated the ability to generalize to a portion of the testing images. However, its fine-tuned counterpart, Cellpose 2.0, exhibited a notable performance degradation, as it could only segment images present in the training set, while losing its previous capability to handle unseen images. The winning algorithm addressed this issue by implementing a simple yet effective strategy known as cell memory replay [32], aiming to re-learn the existing data during fine-tuning. More specifically, the fine-tuning procedure involved combining images from both the existing dataset and the new dataset as a mini-batch for training the model, allowing the algorithm to retain its competence in handling both known and novel images.

To promote the widespread applicability of the new SOTA algorithms, all top-performing teams have made their algorithms publicly available on GitHub, complete with comprehensive preprocessing, training, and testing code. However, a critical challenge remains in bridging the gap between these advanced algorithms and their seamless integration into daily biological practice, as it often demands a basic level of computational expertise to apply these algorithms to new images successfully. To bridge this gap, we invited the top three best-performing teams to integrate their algorithms into Napari [44], an open-source interface specifically designed for user-friendly biological image visualization and analysis. In this way, users gain convenient access to these high-performing algorithms, enabling them to effortlessly apply the segmentation techniques to their own images without necessitating additional coding. Furthermore, to facilitate even greater accessibility and ease of use, the algorithm Docker containers were thoughtfully released. This strategic move empowers users to perform batch image segmentation with utmost simplicity, as a single-line command suffices to initiate the process.

This work has certain limitations that warrant acknowledgment. While the challenge dataset was indeed diverse, it was confined to 2D microscopy images due to the available datasets. However, three-dimensional (3D) microscopy images are becoming increasingly prevalent [45]–[47], which pose new segmentation challenges, such as the large-scale volume and anisotropic resolutions. Moreover, the incorporation of Napari cell segmentation interfaces enhanced accessibility for biologists. Nevertheless, it is crucial to recognize that these algorithms lack the ability to interact with human feedback. Future work should expand the benchmark to more challenging 3D images and build a biologist-in-the-loop system, facilitating seamless collaboration between algorithms and human experts.

In conclusion, the challenge results present a successful proof of concept of generalist cell segmentation algorithms, benefiting from the collective expertise of both biological imaging and machine learning experts. The Transformer-based algorithm surpassed previous SOTA methods by a large margin, which can efficiently generate accurate cell contours on a wide range of microscopy images without user intervention. Furthermore, the top algorithms have been made open-source and seamlessly integrated into user-friendly interfaces. This integration holds great potential for accelerating microscopy image analysis throughput and fostering new discoveries in quantitative biological research. We aim to establish this challenge as a sustainable benchmark platform and we enthusiastically welcome contributions of various new data to expand the data diversity, paving the way for continuous advancement in this vital field.

Author Affiliations

Jun Ma is with the Department of Laboratory Medicine and Pathobiology, University of Toronto; Peter Munk Cardiac Centre, University Health Network; Vector Institute

Ronald Xie is with the Department of Molecular Genetics, University of Toronto; Peter Munk Cardiac Centre, University Health Network; Vector Institute

Shamini Ayyadthury is with the Donnelly Centre, University of Toronto, Toronto, ON, Canada; Princess Margaret Cancer Centre, University Health Network, Toronto, ON, Canada

Cheng Ge is with the School of Medicine and Pharmacy, Ocean University of China

Anubha Gupta is with Indraprastha Institute of Information Technology-Delhi (IIIT-Delhi)

Ritu Gupta is with Institute Rotary Cancer Hospital of All India Institute of Medical Sciences, New Delhi

Song Gu is with the Department of Image Reconstruction, Nanjing Anke Medical Technology Co., Ltd.

Yao Zhang is with Shanghai Artificial Intelligence Laboratory

Gihun Lee and Joonkee Kim are with the Graduate School of AI, KAIST

Wei Lou is with Shenzhen Research Institute of Big Data, The Chinese University of Hongkong (Shenzhen)

Haofeng Li is with Shenzhen Research Institute of Big Data

Eric Upschulte and Timo Dickscheid are with the Institute of Neuroscience and Medicine (INM-1), Research Center Jülich

José Guilherme de Almeida was affiliated with the European Molecular Biology Laboratory, European Bioinformatics Institute (EMBL-EBI). Present address: Champalimaud Foundation—Centre for the Unknown, Lisbon, Portugal

Yixin Wang is with the Department of Bioengineering, Stanford University

Lin Han is with the University of New York

Xin Yang is with the School of Biomedical Engineering, Health Science Center, Shenzhen University

Marco Labagnara and Sahand Jamal Rahi are with École Polytechnique Fédérale de Lausanne

Carly Kempster and Alice Pollitt are with the School of Biological Sciences, University of Reading

Leon Espinosa and Târn Mignot are with CNRS-Aix-Marseille University

Jan Moritz Middeke is with the Medizinische Klinik, Technical University Dresden

Jan-Niklas Eckardt is with the Department of internal medicine, University Hospital Carl Gustav Carus, Technical University Dresden

Wangkai Li is with the Department of Automation, University of Science and Technology of China, School of Information Science and Technology

Zhaoyang Li is with the Institute of advanced technology, University of Science and Technology of China

Xiaochen Cai is with the Department of Computer Science and Technology, Nanjing University

Bizhe Bai is with the School of EECS, The University of Queensland

Noah F. Greenwald is with the School of Medicine, Stanford University

David Van Valen is with the Department of Biology and Bioengineering, Caltech

Erin Weisbart and Beth A. Cimini are with the Imaging Platform, Broad Institute of MIT and Harvard

Zhuoshi Li and Chao Zuo are with Nanjing University of Science and Technology

Oscar Brück is with Hematoscope Lab, Comprehensive Cancer Center & Center of Diagnostics, Helsinki University Hospital & University of Helsinki

Gary D. Bader is with the Donnelly Centre and Department of Molecular Genetics, University of Toronto

Bo Wang is with the Peter Munk Cardiac Centre, University Health Network; Department of Laboratory Medicine and Pathobiology and Department of Computer Science, University of Toronto; Vector Institute

METHODS

Challenge Organization

This challenge was pre-registered in the Thirty-sixth Conference on Neural Information Processing Systems (NeurIPS) (<https://neurips.cc/Conferences/2022/CompetitionTrack>) following a peer review process conducted by the competition program committee comprising experts in both machine learning and challenges organization. The challenge was officially launched on June 15, 2022, and ran for 139 days until October 31, 2022, marking the testing submission deadline. Throughout the development phase, participants were given the opportunity to submit their tuning set segmentation results on the challenge platform and obtain corresponding F1 scores. Moreover, to minimize entry barriers, we supplied a U-Net-based baseline model and offered a step-by-step tutorial to assist participants in becoming familiar with model training, inference, and submission. Additionally, we furnished guidelines and suggestions on state-of-the-art cell segmentation methods [6], [9], [12], [13], empowering participants to surpass the baseline and achieve higher levels of performance.

Dataset curation and pre-processing

The images were curated from multiple laboratories, each specializing in different cell types and modalities. Part of the training images was obtained from publicly available datasets with proper license permits or approval from the respective authors. Detailed information regarding these images can be found in Supplementary Table 1-3. It should be noted that none of the testing images had been previously made public, ensuring the avoidance of potential data or label leakage.

The original image formats included png, bmp, jpg, tif, tiff, npy, and npz. The npy and npz formats, which are not typical image formats, were converted to the widely used png format. All other image formats were retained as they were, to accommodate the diverse array of image formats that the developed algorithms might encounter. External datasets and pre-trained models are allowed, but participants should post the corresponding links to the competition forum and we also maintained a document of external datasets on the challenge homepage to make sure these external datasets were available to all participants.

For the labeled dataset, all the cells were annotated in each image, with the exception of red blood cells in blood and bone marrow slides since biomedical researchers predominantly centered on the stained leukocytes. The annotation team consisted of two biologists with 10 years of experience, responsible for ensuring compliance with annotation requirements. In cases where data contributors provided cell annotations, the annotations were thoroughly checked and revised as needed. For contributors who provided unlabeled images, publicly available specialist models [6], [8], [10], [11] were initially employed to generate predictions. The resulting segmentation outcomes were subsequently subjected to manual revision by the biologists. Additionally, to maintain the quality and reliability of the dataset, each image-annotation pair underwent stringent quality control. Images with less than five cells were excluded from the dataset, and cells containing fewer than 15 pixels were also removed.

Top three best-performing algorithms

Best-performing algorithm. Lee et al. [29] (T1-osilab) incorporated model-centric and data-centric approaches to learn generalizable representations for heterogeneous microscopy image modalities and achieved a good trade-off between model accuracy and efficiency. From the model-centric perspective, the framework adopted a typical encoder-decoder architecture to extract hierarchical features and integrate them through skip connections. Concretely, SegFormer [30] served as the encoder, while MA-Net [31] was employed as the decoder, utilizing the Mish [48] activation function. The network jointly predicted cell probability maps and regressed cell-wise vertical and horizontal gradient flows, followed by a gradient tracking post-processing to separate touched cells. From the data-centric perspective, they tailored two cell-aware augmentations to extensively enrich the diversity of the dataset and combined them with commonly used intensity and spatial augmentation methods to improve model generalization. Specifically, image intensities were randomized in a cell-wise manner and cell boundary pixels were excluded to separate the crowded cells. Moreover, a two-phase pre-training and fine-tuning pipeline was used to retrain the knowledge from external datasets, including TissueNet [6], OmniPose [9], CellPose [12], and LiveCell [49]. Furthermore, to address minor modalities, they were selected through unsupervised clustering with the latent embedding and subsequently over-sampled during training, thereby aiming to enhance the performance of these less-represented modalities.

The overall loss function was the combination of binary cross-entropy loss and mean-square error loss. The inference process relied on the sliding window strategy, a highly efficient approach for processing whole-slide images. During the merging of predictions from these small window patches, an importance map was generated and applied to the predictions, thereby preventing the recognition of the same cells at the patch boundary as multiple cells. The comprehensive integration of these approaches resulted in exceptional performance, effectively handling diverse microscopy image modalities with high accuracy.

Second-best-performing algorithm. Lou et al. [33] (T2-sribdmed) designed a classification-and-segmentation framework that first classified the input image into one group and then performed cell segmentation with a model trained for that group. The classification pipeline consisted of three steps. First, it employed a segmentation model trained on labeled images to generate pseudo labels for unlabeled images. Second, the images were classified into four groups based on image intensities. Specifically, the first class included all single-channel images. The three-channel RGB images were converted to Hue, Saturation, and Value (HSV) color space. Within this transformed domain, images exhibiting a mean saturation (S) greater than 0.1 and a mean value (V) falling within the range [0.1, 0.6] were assigned to the second class. The remaining images with cell areas larger than 8000 pixels were classified as the third class, while others were designated as the fourth class. Finally, a ResNet18 [50] was trained for automated group classification. The segmentation network followed a design of U-Net-like architecture, where the encoder was ConvNeXt [34]. Motivated by the observation that most cells in the first and second classes were roundish, a decoder with star-convex polygon-based cell representation [51] was integrated with the encoder for cell instance segmentation, termed as ConvNeXt-Stardist. The non-maximum suppression (NMS) [52] was employed in the post-processing to remove duplicated predictions. For the third and fourth classes, the prediction head in HoverNet [53] was adopted as the decoder, termed as ConvNeXt-Hover. The marker-based watershed algorithm was applied in the post-processing phase to separate touching cells.

There were four segmentation models in total trained for four image groups respectively. ConvNeXt-Stardist was trained with a combination of cross-entropy loss, Dice loss, and MAE loss, and ConvNeXt-Hover was trained with a combination of cross-entropy loss, Dice loss, MSE loss, and mean squared gradient error loss. Both ConvNeXt-Stardist and ConvNeXt-Hover were pre-trained on all images and finetuned on the images from the corresponding group. During inference, the input image was first classified into certain groups by the classification model and then processed by the segmentation model trained for the group.

Third-best-performing algorithm. Upschulte et al. [35] (T3-cells) proposed a Contour Proposal Network (CPN) [54], which treated instance segmentation as a sparse detection problem by regressing object contours anchored at pixel locations.

This enabled the model to handle multiple objects assigned to the same pixel and recover partially superimposed objects accurately. The shape-focused nature of contour representation learning also facilitated the development of inductive shape priors, potentially improving robustness in challenging conditions.

The CPN utilized the ResNeXt backbone network [36] to extract multiscale feature maps, a regression head to generate candidate contour representations for each pixel, and a classification head to determine whether an object was present or not at these locations. A proposal sampling stage extracted a sparse list of contour representations, which were transformed into the pixel domain using differentiable Fourier transformation to encode contour information in the frequency domain [55]. The precision of the contours was further improved by using a displacement field generated by an additional regression head. In addition to the original CPN, this work introduced dedicated supervision for boundaries and proposed an extra branch to estimate localization uncertainty for boundaries. The multitask training objective was defined by a combination of the average absolute difference loss for contour regression, the generalized IoU loss for boundary localization [56], the absolute L1 distance for local refinement [54], the distance loss for frequency regularization [54], the binary cross entropy loss for classification, and the negative power log-likelihood loss for uncertainty estimation [57].

The uncertainty-aware Listen2Student mechanism [58] was applied to incorporate unlabeled examples during training, where a teacher model generated bounding boxes as pseudo-labels to supervise the student model. For post-processing, the Vanilla NMS relying solely on the classification score might not reliably indicate the proposal’s quality. To address this issue, the approach proposed in [57] was employed to incorporate uncertainty estimations into the NMS selection process. The object contours were transformed into segmentation masks through rasterization and region filling. A region-growing technique [59] was further adopted for overlapping regions.

Existing SOTA cell segmentation algorithms

The following methods were designed for grey and two-channel microscopy images, while the challenge dataset was curated for developing universal algorithms that were agnostic to different image channel formats. Thus, we preprocess the challenge images to grey images by the ‘skimage.color.rgb2gray’ function.

Cellpose [12] was the first generalist algorithm for microscopy image segmentation. It used U-Net to predict horizontal and vertical gradient maps of cell instances and a foreground binary mask, which can handle irregular cell shapes. Individual cell labels can be recovered by gradient tracking-based postprocessing. To evaluate the pre-trained Cellpose model on the challenge testing set, we chose the most generalizable ‘cyto2’ model, which was trained on Cellpose dataset and user-submitted images.

Omnipose [9] was an extension of Cellpose, aiming to handle very elongated cells, especially bacterial cells. The network architecture backbone was still U-Net but the model had four heads to predict four components: two gradient flows, a distance transform map, and a boundary map. We also chose the ‘cyto2’ model to infer the challenge testing images.

Cellpose 2.0 [13] further enhanced the usability of Cellpose for fast customization. It allowed users to train customized cellular segmentation models with 100-200 user-annotated regions of interest by fine-tuning the pre-trained Cellpose Model. The network architecture in Cellpose 2.0 was the same as the Cellpose model.

KIT-GE [37] trained a U-Net model to predict cell distance and neighbor distance, followed by watershed post-processing. Compared to the original U-Net [22], the maximum pooling layers were replaced with 2D convolutional layers with stride 2, and batch normalization layers were added after the convolutional layers.

Evaluation metrics

This challenge focused on two key metrics: segmentation accuracy and efficiency. While segmentation accuracy is a fundamental metric in cell segmentation, we included efficiency in the evaluation to account for its significance during model deployment. If the challenge metrics only considered the algorithm accuracy, participants may solely prioritize it by employing the ensemble of multiple models [18]. However, such solutions may not be practical in real-world scenarios, particularly for biologists who typically have limited computational resources. Recognizing this, we incorporated efficiency as an evaluation metric to guide participants in considering the trade-off between model accuracy and efficiency.

Segmentation accuracy metric: F1 score. Cell segmentation is a typical instance segmentation task. We employed the widely used F1 Score to evaluate the segmentation results [6], [60], [61]. Specifically, each predicted cell mask is matched to the most similar ground-truth mask based on the predefined intersection over union (IoU) threshold (i.e., 0.5). A predicted cell mask is classified as correct segmentation as long as its IoU is over the predefined IoU threshold. A higher threshold requires a larger overlap between the predicted cell mask and the ground-truth mask, and a commonly used threshold is 0.5. Then, all the cells can be divided into three categories, including true positives (TP), false positives (FP), and false negatives (FN). TP denotes correctly segmented cells. FP denotes wrong segmented cells while FN denotes missed cells in the segmentation mask. After that, we can compute the precision and recall, which are defined by $precision = \frac{TP}{TP+FP}$ and $recall = \frac{TP}{TP+FN}$, respectively. The F1 score can be interpreted as a harmonic mean of the precision and recall, which is defined by

$$F1 = \frac{2 \times Precision \times recall}{precision + recall}.$$

Since the cells located in the boundaries are usually incomplete and have low practical value in various downstream analysis tasks, we remove these cells when computing the metrics.

Segmentation efficiency metric: Running time. All the submitted Docker containers were run on the same desktop workstation with a 12-core CPU, 32GB RAM, and one NVIDIA 2080Ti GPU. In order to obtain the running time T for each image, the testing images were segmented one by one. To compensate for the Docker container startup time, we gave a time tolerance for the running time. Specifically, the time tolerance was 10s if the image size (height $H \times$ width W) was no more than 1,000,000. If the image size was more than 1,000,000, the time tolerance was $(H \times W)/1000000 \times 10s$. This time tolerance was determined by the open-source U-Net baseline.

Ranking Scheme: Rank-then-aggregate

Both F1 score and running time will be used for ranking. However, the two metrics cannot be directly fused because they have different dimensions. Thus, we will use a “rank-then-aggregate” scheme for ranking, including the following three steps:

- Step 1. Computing the two metrics for each testing case and each team;
- Step 2. Ranking teams for each of the N testing cases such that each team obtains $N \times 2$ rankings;
- Step 3. Computing ranking scores for all teams by averaging all these rankings and then normalizing them by the number of teams. The final rank will be determined by the mean ranking scores.

In addition to the employed rank-then-aggregate scheme, several other strategies can be used to obtain a ranking, but these may lead to different orderings of algorithms and thus different winners [62]. A typical ranking scheme was “aggregate-then-rank”: computing mean scores across all testing cases for each team and then using this aggregation to rank each team. One can also use test-based procedures for ranking. Specifically, each pair of algorithms are compared by statistical hypothesis tests. The ranking is then performed according to the resulting relations or according to the number of significant one-sided test results. In the latter case, if algorithms have the same number of significant test results, then they obtain the same rank. For analysis purposes, we computed the ranks of the 28 algorithms based on five different ranking schemes: mean-then-rank, median-then-rank, rank-then-mean, rank-then-median, and statistical significance test-based ranking.

Importantly, for a transparent challenge, the evaluation code and ranking scheme were publicly available at the beginning of the challenge. For comparative analysis, we applied different ranking schemes to the 28 algorithms, including rank-then-mean, rank-then-median, median-then-rank, mean-then-rank, and test-based rank. It can be found that most algorithms had fluctuations under different ranking schemes but the winning algorithm consistently held the first place.

Ranking Stability and statistical analysis

Ranking stability is an important factor for robust challenge results [63]. Thus, we applied bootstrapping and computed Kendall’s τ [64] to quantitatively analyze the variability of our ranking scheme. Specifically, we first extracted 1000 bootstrap samples from the international validation set and computed the ranks again for each bootstrap sample. Then, the ranking agreement was quantified by Kendall’s τ . Kendall’s τ computes the number of pairwise concordances and discordances between ranking lists. Its value ranges $[-1, 1]$ where -1 and 1 denote inverted and identical order, respectively. A stable ranking scheme should have a high Kendall’s τ value that is close to 1. To compare the performance of different algorithms, we performed Wilcoxon signed rank test because it is a paired comparison. Results were considered statistically significant if the p – value is less than 0.05.

Data availability

The dataset has been publicly available on the challenge website <https://neurips22-cellseg.grand-challenge.org/>.

Code availability

The top ten teams have made their code publicly available at GitHub <https://neurips22-cellseg.grand-challenge.org/awards/>. The code of metrics and the evaluation of existing cell segmentation algorithms are available at <https://github.com/JunMa11/NeurIPS-CellSeg>. The Napari interface and huggingface online segmentation tool for the top three best-performing algorithms are available at T1-osilab: <https://github.com/joonkeekim/mediar-napari>; T2-sribdmed: https://github.com/Lewislou/cellseg_sribd_napari; T3-cells: <https://github.com/FZJ-INM1-BDA/celldetection-napari>.

Acknowledgements

This work was supported by the Natural Sciences and Engineering Research Council of Canada (NSERC, RGPIN-2020-06189 and DGECR-2020-00294), Canadian Institute for Advanced Research (CIFAR) AI Catalyst Grants, and CIFAR AI Chair programs. We thank Patrick Byrne, Maria Kost-Alimova, Shantanu Singh, and Anne E. Carpenter for contributing U2OS and adipocyte images. We thank Dr. Andrea J. Radtke and Dr. Ronald Germain for contributing adenoid and tonsil whole-slide fluorescent images. We thank Sweta Banerjee for providing multiple myeloma plasma cell annotations

in stained brightfield images. The platelet differential interference contrast images collected by Carly Kempster and Alice Pollitt were supported by the British Heart Foundation/NC3Rs (NC/S001441/1) Grant. Anubha Gupta would like to thank the Department of Science and Technology, Govt. of India for the SERB-POWER fellowship (Grant No.: SPF/2021/000209) and the Infosys Centre for AI, IIT-Delhi for the financial support to run this challenge.

Competing interests

Song Gu is employed by Nanjing Anke Medical Technology Co., Ltd. All other authors have no competing interests.

REFERENCES

- [1] H. W. Jackson, J. R. Fischer, V. R. Zanotelli, H. R. Ali, R. Mechera, S. D. Soysal, H. Moch, S. Muenst, Z. Varga, W. P. Weber *et al.*, "The single-cell pathology landscape of breast cancer," *Nature*, vol. 578, no. 7796, pp. 615–620, 2020.
- [2] L. Capolupo, I. Khven, A. R. Lederer, L. Mazzeo, G. Glousker, S. Ho, F. Russo, J. P. Montoya, D. R. Bhandari, A. P. Bowman, S. R. Ellis, R. Guiet, O. Burri, J. Detzner, J. Muthing, K. Homicsko, F. Kuonen, M. Gilliet, B. Spengler, R. M. A. Heeren, G. P. Dotto, G. L. Manno, and G. D'Angelo, "Sphingolipids control dermal fibroblast heterogeneity," *Science*, vol. 376, no. 6590, p. eabh1623, 2022.
- [3] J.-R. Lin, S. Wang, S. Coy, Y.-A. Chen, C. Yapp, M. Tyler, M. K. Nariya, C. N. Heiser, K. S. Lau, S. Santagata, and P. K. Sorger, "Multiplexed 3d atlas of state transitions and immune interaction in colorectal cancer," *Cell*, vol. 186, no. 2, pp. 363–381, 2023.
- [4] R. Hollandi, N. Moshkov, L. Paavolainen, E. Tasnadi, F. Piccinini, and P. Horvath, "Nucleus segmentation: towards automated solutions," *Trends in Cell Biology*, 2022.
- [5] E. Moen, D. Bannon, T. Kudo, W. Graf, M. Covert, and D. Van Valen, "Deep learning for cellular image analysis," *Nature Methods*, vol. 16, no. 12, pp. 1233–1246, 2019.
- [6] N. F. Greenwald, G. Miller, E. Moen, A. Kong, A. Kagel, T. Dougherty, C. C. Fullaway, B. J. McIntosh, K. X. Leow, M. S. Schwartz *et al.*, "Whole-cell segmentation of tissue images with human-level performance using large-scale data annotation and deep learning," *Nature Biotechnology*, pp. 1–11, 2021.
- [7] M. Y. Lee, J. S. Bedia, S. S. Bhate, G. L. Barlow, D. Phillips, W. J. Fantl, G. P. Nolan, and C. M. Schürch, "Cellseg: a robust, pre-trained nucleus segmentation and pixel quantification software for highly multiplexed fluorescence images," *BMC Bioinformatics*, vol. 23, no. 1, pp. 1–17, 2022.
- [8] C. Kempster, G. Butler, E. Kuznecova, K. A. Taylor, N. Kriek, G. Little, M. A. Sowa, T. Sage, L. J. Johnson, J. M. Gibbins *et al.*, "Fully automated platelet differential interference contrast image analysis via deep learning," *Scientific Reports*, vol. 12, no. 1, pp. 1–13, 2022.
- [9] K. J. Cutler, C. Stringer, T. W. Lo, L. Rappez, N. Stroustrup, S. Brook Peterson, P. A. Wiggins, and J. D. Mougous, "Omnipose: a high-precision morphology-independent solution for bacterial cell segmentation," *Nature Methods*, vol. 19, no. 11, pp. 1438–1448, 2022.
- [10] D. Bunk, J. Moriasy, F. Thoma, C. Jakubke, C. Osman, and D. Hörl, "Yeastmate: neural network-assisted segmentation of mating and budding events in *saccharomyces cerevisiae*," *Bioinformatics*, vol. 38, no. 9, pp. 2667–2669, 2022.
- [11] N. Dietler, M. Minder, V. Gligorovski, A. M. Economou, D. A. H. L. Joly, A. Sadeghi, C. H. M. Chan, M. Koziński, M. Weigert, A.-F. Bitbol *et al.*, "A convolutional neural network segments yeast microscopy images with high accuracy," *Nature Communications*, vol. 11, no. 1, pp. 1–8, 2020.
- [12] C. Stringer, T. Wang, M. Michaelos, and M. Pachitariu, "Cellpose: a generalist algorithm for cellular segmentation," *Nature Methods*, vol. 18, no. 1, pp. 100–106, 2021.
- [13] M. Pachitariu and C. Stringer, "Cellpose 2.0: how to train your own model," *Nature Methods*, vol. 19, no. 12, pp. 1634–1641, 2022.
- [14] J. Deng, W. Dong, R. Socher, L.-J. Li, K. Li, and L. Fei-Fei, "Imagenet: A large-scale hierarchical image database," in *IEEE Conference on Computer Vision and Pattern Recognition*, 2009, pp. 248–255.
- [15] W. Bulten, K. Kartasalo, P.-H. C. Chen, P. Ström, H. Pinckaers, K. Nagpal, Y. Cai, D. F. Steiner, H. van Boven, R. Vink *et al.*, "Artificial intelligence for diagnosis and gleason grading of prostate cancer: the panda challenge," *Nature Medicine*, vol. 28, no. 1, pp. 154–163, 2022.
- [16] V. Ulman, M. Maška, K. E. Magnusson, O. Ronneberger, C. Haubold, N. Harder, P. Matula, P. Matula, D. Svoboda, M. Radojevic *et al.*, "An objective comparison of cell-tracking algorithms," *Nature Methods*, vol. 14, no. 12, pp. 1141–1152, 2017.
- [17] M. Maška, V. Ulman, P. Delgado-Rodriguez, E. Gómez-de Mariscal, T. Nečasová, F. A. Guerrero Peña, T. I. Ren, E. M. Meyerowitz, T. Scherr, K. Löffler *et al.*, "The cell tracking challenge: 10 years of objective benchmarking," *Nature Methods*, pp. 1–11, 2023.
- [18] J. C. Caicedo, A. Goodman, K. W. Karhohs, B. A. Cimini, J. Ackerman, M. Haghighi, C. Heng, T. Becker, M. Doan, C. McQuinn *et al.*, "Nucleus segmentation across imaging experiments: the 2018 data science bowl," *Nature Methods*, vol. 16, no. 12, pp. 1247–1253, 2019.
- [19] N. Tajbakhsh, L. Jeyaseelan, Q. Li, J. N. Chiang, Z. Wu, and X. Ding, "Embracing imperfect datasets: A review of deep learning solutions for medical image segmentation," *Medical Image Analysis*, vol. 63, p. 101693, 2020.
- [20] J. Ma and B. Wang, "Towards foundation models of biological image segmentation," *Nature Methods*, vol. 20, no. 7, pp. 953–955, 2023.
- [21] A. Gupta, S. Gehlot, S. Goswami, S. Motwani, R. Gupta, Á. G. Faura, D. Štepec, T. Martinčič, R. Azad, D. Merhof *et al.*, "Segpc-2021: A challenge & dataset on segmentation of multiple myeloma plasma cells from microscopic images," *Medical Image Analysis*, vol. 83, p. 102677, 2023.
- [22] O. Ronneberger, P. Fischer, and T. Brox, "U-net: Convolutional networks for biomedical image segmentation," in *International Conference on Medical Image Computing and Computer-assisted Intervention*, 2015, pp. 234–241.
- [23] T. Falk, D. Mai, R. Besch, Ö. Çiçek, A. Abdulkadir, Y. Marrakchi, A. Böhm, J. Deubner, Z. Jäckel, K. Seiwald *et al.*, "U-net: deep learning for cell counting, detection, and morphometry," *Nature Methods*, vol. 16, no. 1, pp. 67–70, 2019.
- [24] L.-C. Chen, G. Papandreou, I. Kokkinos, K. Murphy, and A. L. Yuille, "DeepLab: Semantic image segmentation with deep convolutional nets, atrous convolution, and fully connected crfs," *IEEE Transactions on Pattern Analysis and Machine Intelligence*, vol. 40, no. 4, pp. 834–848, 2017.
- [25] A. Vaswani, N. Shazeer, N. Parmar, J. Uszkoreit, L. Jones, A. N. Gomez, Ł. Kaiser, and I. Polosukhin, "Attention is all you need," *Advances in Neural Information Processing Systems*, vol. 30, 2017.
- [26] A. Dosovitskiy, L. Beyer, A. Kolesnikov, D. Weissenborn, X. Zhai, T. Unterthiner, M. Dehghani, M. Minderer, G. Heigold, S. Gelly *et al.*, "An image is worth 16x16 words: Transformers for image recognition at scale," in *International Conference on Learning Representations*, 2020.
- [27] Z. Liu, Y. Lin, Y. Cao, H. Hu, Y. Wei, Z. Zhang, S. Lin, and B. Guo, "Swin transformer: Hierarchical vision transformer using shifted windows," in *Proceedings of the IEEE/CVF International Conference on Computer Vision*, 2021, pp. 10 012–10 022.
- [28] X. Li, Y. Zhang, J. Wu, and Q. Dai, "Challenges and opportunities in bioimage analysis," *Nature Methods*, vol. 20, no. 7, pp. 958–961, 2023.
- [29] G. Lee, S. Kim, J. Kim, and S.-Y. Yun, "Mediar: Harmony of data-centric and model-centric for multi-modality microscopy," in *Proceedings of The Cell Segmentation Challenge in Multi-modality High-Resolution Microscopy Images*, vol. 212, 2023, pp. 1–16.
- [30] E. Xie, W. Wang, Z. Yu, A. Anandkumar, J. M. Alvarez, and P. Luo, "Segformer: Simple and efficient design for semantic segmentation with transformers," *Advances in Neural Information Processing Systems*, vol. 34, 2021.
- [31] T. Fan, G. Wang, Y. Li, and H. Wang, "Ma-net: A multi-scale attention network for liver and tumor segmentation," *IEEE Access*, vol. 8, pp. 179 656–179 665, 2020.

- [32] A. Chaudhry, A. Gordo, P. Dokania, P. Torr, and D. Lopez-Paz, "Using hindsight to anchor past knowledge in continual learning," in *Proceedings of the AAAI Conference on Artificial Intelligence*, vol. 35, no. 8, 2021, pp. 6993–7001.
- [33] W. Lou, X. Yu, C. Liu, X. Wan, G. Li, S. Liu, and H. Li, "Multi-stream cell segmentation with low-level cues for multi-modality images," in *Proceedings of The Cell Segmentation Challenge in Multi-modality High-Resolution Microscopy Images*, vol. 212, 2023, pp. 1–10.
- [34] Z. Liu, H. Mao, C.-Y. Wu, C. Feichtenhofer, T. Darrell, and S. Xie, "A convnet for the 2020s," in *Proceedings of the IEEE/CVF Conference on Computer Vision and Pattern Recognition (CVPR)*, 2022, pp. 11 976–11 986.
- [35] E. Upschulte, S. Harmeling, K. Amunts, and T. Dickscheid, "Uncertainty-aware contour proposal networks for cell segmentation in multi-modality high-resolution microscopy images," in *Proceedings of The Cell Segmentation Challenge in Multi-modality High-Resolution Microscopy Images*, vol. 212, 2023, pp. 1–12.
- [36] S. Xie, R. Girshick, P. Dollár, Z. Tu, and K. He, "Aggregated residual transformations for deep neural networks," in *Proceedings of the IEEE Conference on Computer Vision and Pattern Recognition*, 2017, pp. 1492–1500.
- [37] T. Scherr, K. Löffler, M. Böhlend, and R. Mikut, "Cell segmentation and tracking using cnn-based distance predictions and a graph-based matching strategy," *PLoS One*, vol. 15, no. 12, p. e0243219, 2020.
- [38] G. I. Parisi, R. Kemker, J. L. Part, C. Kanan, and S. Wermter, "Continual lifelong learning with neural networks: A review," *Neural Networks*, vol. 113, pp. 54–71, 2019.
- [39] F. A. G. Pena, P. D. M. Fernandez, P. T. Tarr, T. I. Ren, E. M. Meyerowitz, and A. Cunha, "J regularization improves imbalanced multiclass segmentation," in *IEEE 17th International Symposium on Biomedical Imaging*, 2020, pp. 1–5.
- [40] F. Isensee, P. F. Jaeger, S. A. Kohl, J. Petersen, and K. H. Maier-Hein, "nnu-net: a self-configuring method for deep learning-based biomedical image segmentation," *Nature Methods*, vol. 18, no. 2, pp. 203–211, 2021.
- [41] K. He, G. Gkioxari, P. Dollár, and R. Girshick, "Mask r-cnn," in *Proceedings of the IEEE International Conference on Computer Vision*, 2017, pp. 2961–2969.
- [42] L. Wangkai, L. Zhaoyang, S. Rui, M. Huayu, L. Naisong, Y. Wang, P. Yuwen, X. Guoxin, L. Huakai, X. Zhiwei, and Z. Tianzhu, "Maunet: Modality-aware anti-ambiguity u-net for multi-modality cell segmentation," in *Proceedings of The Cell Segmentation Challenge in Multi-modality High-Resolution Microscopy Images*, ser. Proceedings of Machine Learning Research, vol. 212, 2023, pp. 1–12.
- [43] A. Bochkovskiy, C.-Y. Wang, and H.-Y. M. Liao, "Yolov4: Optimal speed and accuracy of object detection," *arXiv preprint arXiv:2004.10934*, 2020.
- [44] N. Sofroniew, T. Lambert, K. Evans, J. Nunez-Iglesias, G. Bokota, P. Winston, G. Peña-Castellanos, K. Yamauchi, M. Bussonnier, D. Doncila Pop, A. Can Solak, Z. Liu, P. Wadhwa, A. Burt, G. Buckley, A. Sweet, L. Migas, V. Hilsenstein, L. Gaifas, J. Bragantini, J. Rodríguez-Guerra, H. Muñoz, J. Freeman, P. Boone, A. Lowe, C. Gohlke, L. Royer, A. PIERRÉ, H. Har-Gil, and A. McGovern, "napari: a multi-dimensional image viewer for Python," 2022.
- [45] S. Fu, W. Shi, T. Luo, Y. He, L. Zhou, J. Yang, Z. Yang, J. Liu, X. Liu, Z. Guo *et al.*, "Field-dependent deep learning enables high-throughput whole-cell 3d super-resolution imaging," *Nature Methods*, vol. 20, no. 3, pp. 459–468, 2023.
- [46] Z. Zhao, Y. Zhou, B. Liu, J. He, J. Zhao, Y. Cai, J. Fan, X. Li, Z. Wang, Z. Lu *et al.*, "Two-photon synthetic aperture microscopy for minimally invasive fast 3d imaging of native subcellular behaviors in deep tissue," *Cell*, vol. 186, no. 11, pp. 2475–2491, 2023.
- [47] X. Li, Y. Wu, Y. Su, I. Rey-Suarez, C. Matthaeus, T. B. Updegrove, Z. Wei, L. Zhang, H. Sasaki, Y. Li *et al.*, "Three-dimensional structured illumination microscopy with enhanced axial resolution," *Nature Biotechnology*, pp. 1–13, 2023.
- [48] D. Misra, "Mish: A self regularized non-monotonic activation function," 2020.
- [49] C. Edlund, T. R. Jackson, N. Khalid, N. Bevan, T. Dale, A. Dengel, S. Ahmed, J. Trygg, and R. Sjögren, "Livecell—a large-scale dataset for label-free live cell segmentation," *Nature Methods*, vol. 18, no. 9, pp. 1038–1045, 2021.
- [50] K. He, X. Zhang, S. Ren, and J. Sun, "Deep residual learning for image recognition," in *Proceedings of the IEEE Conference on Computer Vision and Pattern Recognition*, 2016, pp. 770–778.
- [51] U. Schmidt, M. Weigert, C. Broaddus, and G. Myers, "Cell detection with star-convex polygons," in *Medical Image Computing and Computer Assisted Intervention – MICCAI 2018*, 2018, pp. 265–273.
- [52] S. Ren, K. He, R. Girshick, and J. Sun, "Faster r-cnn: Towards real-time object detection with region proposal networks," in *Advances in Neural Information Processing Systems*, vol. 28, 2015.
- [53] S. Graham, Q. D. Vu, S. E. A. Raza, A. Azam, Y. W. Tsang, J. T. Kwak, and N. Rajpoot, "Hover-net: Simultaneous segmentation and classification of nuclei in multi-tissue histology images," *Medical Image Analysis*, vol. 58, p. 101563, 2019.
- [54] E. Upschulte, S. Harmeling, K. Amunts, and T. Dickscheid, "Contour proposal networks for biomedical instance segmentation," *Medical Image Analysis*, vol. 77, p. 102371, 2022.
- [55] F. P. Kuhl and C. R. Giardina, "Elliptic fourier features of a closed contour," *Computer Graphics and Image Processing*, vol. 18, no. 3, pp. 236–258, 1982.
- [56] H. Rezatofighi, N. Tsoi, J. Gwak, A. Sadeghian, I. Reid, and S. Savarese, "Generalized intersection over union: A metric and a loss for bounding box regression," in *Proceedings of the IEEE/CVF Conference on Computer Vision and Pattern Recognition (CVPR)*, 2019.
- [57] Y. Lee, J.-W. Hwang, H.-I. Kim, K. Yun, Y. Kwon, Y. Bae, and S. J. Hwang, "Localization uncertainty estimation for anchor-free object detection," in *Computer Vision – ECCV 2022 Workshops*, 2023, pp. 27–42.
- [58] Y.-C. Liu, C.-Y. Ma, and Z. Kira, "Unbiased teacher v2: Semi-supervised object detection for anchor-free and anchor-based detectors," in *Proceedings of the IEEE/CVF Conference on Computer Vision and Pattern Recognition (CVPR)*, June 2022, pp. 9819–9828.
- [59] R. Adams and L. Bischof, "Seeded region growing," *IEEE Transactions on pattern analysis and machine intelligence*, vol. 16, no. 6, pp. 641–647, 1994.
- [60] L. Maier-Hein, A. Reinke, E. Christodoulou, B. Glocker, P. Godau, F. Isensee, J. Kleesiek, M. Kozubek, M. Reyes, M. A. Riegler *et al.*, "Metrics reloaded: Pitfalls and recommendations for image analysis validation," *arXiv preprint arXiv:2206.01653*, 2022.
- [61] D. Hirling, E. Tasnadi, J. Caicedo, M. V. Caroprese, R. Sjögren, M. Aubreville, K. Koos, and P. Horvath, "Segmentation metric misinterpretations in bioimage analysis," *Nature Methods*, pp. 1–4, 2023.
- [62] L. Maier-Hein, M. Eisenmann, A. Reinke, S. Onogur, M. Stankovic, P. Scholz, T. Arbel, H. Bogunovic, A. P. Bradley, A. Carass *et al.*, "Why rankings of biomedical image analysis competitions should be interpreted with care," *Nature Communications*, vol. 9, no. 1, p. 5217, 2018.
- [63] M. Wiesenfarth, A. Reinke, B. A. Landman, M. Eisenmann, L. A. Saiz, M. J. Cardoso *et al.*, "Methods and open-source toolkit for analyzing and visualizing challenge results," *Scientific Reports*, vol. 11, no. 1, pp. 1–15, 2021.
- [64] M. G. Kendall, "A new measure of rank correlation," *Biometrika*, vol. 30, no. 1/2, pp. 81–93, 1938.